nature cell biology

ARTICLES

https://doi.org/10.1038/s41556-018-0247-4

Fluidization-mediated tissue spreading by mitotic cell rounding and non-canonical Wnt signalling

Nicoletta I. Petridou[1], Silvia Grigolon[2], Guillaume Salbreux[2], Edouard Hannezo[1] and Carl-Philipp Heisenberg[1*]

Tissue morphogenesis is driven by mechanical forces that elicit changes in cell size, shape and motion. The extent by which forces deform tissues critically depends on the rheological properties of the recipient tissue. Yet, whether and how dynamic changes in tissue rheology affect tissue morphogenesis and how they are regulated within the developing organism remain unclear. Here, we show that blastoderm spreading at the onset of zebrafish morphogenesis relies on a rapid, pronounced and spatially patterned tissue fluidization. Blastoderm fluidization is temporally controlled by mitotic cell rounding-dependent cell–cell contact disassembly during the last rounds of cell cleavages. Moreover, fluidization is spatially restricted to the central blastoderm by local activation of non-canonical Wnt signalling within the blastoderm margin, increasing cell cohesion and thereby counteracting the effect of mitotic rounding on contact disassembly. Overall, our results identify a fluidity transition mediated by loss of cell cohesion as a critical regulator of embryo morphogenesis.

Embryonic development is brought about by the integration of mechanical and chemical signals, coordinating the transformation of an initially amorphous cell mass into a complex three-dimensional (3D) organism[1,2]. Tissues intrinsically generate and/or extrinsically receive forces and deform in response to these forces depending on their dissipative properties, such as viscosity and elasticity[3,4]. Regulated changes in tissue material properties have been proposed to be important for various morphogenetic processes in vertebrate development, such as body axis elongation[5–7] and germ layer formation[8,9], and to be influenced by alterations in cell cohesion, movement and division[10–12]. Interestingly, although tissue viscosity linearly scales with cell cohesion, this relationship is lost once a critical threshold level of cohesion is reached[10]. Likewise, small changes in cell contractility and/or cohesion can lead to drastic and discontinuous changes in tissue rheology[13–16], resembling tissue solidification/fluidization phase transitions. However, remarkably, little is yet known about whether such phase transitions occur in animal development, how they are achieved on a molecular and cellular level and, most importantly, what their function is within the developing embryo.

Results

Blastoderm fluidizes at the onset of morphogenesis. At the onset of zebrafish development, the blastoderm, composed of deep cells covered by an epithelial enveloping layer (EVL), starts spreading over the yolk in a process called 'doming'[17,18] (Fig. 1a–c). During doming, the blastoderm-to-yolk interface (BYI) bends upwards in the centre and downwards at the margin, reducing the blastoderm height at the centre (Fig. 1d,e and Supplementary Video 1). These tissue shape changes have previously been attributed to two force-generating processes: active EVL expansion, which reduces the blastoderm tissue surface tension (TST), and active deep-cell intercalations, which radially contract the blastoderm[19]. However, when mapping the spatiotemporal evolution of radial deep-cell intercalations during doming, we noted that, at the onset of doming, deep-cell protrusions were not yet preferentially oriented along the radial axis of the blastoderm[19] (Supplementary Fig. 1a,b), suggesting that during doming initiation, radial stress generation is minimal.

The timescale of tissue deformation generally depends on the relationship between active force generation and passive viscoelastic response[20]. Thus, we reasoned that reducing deep-cell tissue resistance to active EVL expansion might constitute a mechanism by which blastoderm deformation is achieved when radial stress generation is minimal. To address this possibility, we performed stress-relaxation experiments using micropipette aspiration (MPA) to map deep-cell tissue material properties[21,22] (see Methods; Supplementary Fig. 1c–h). We found that deep-cell tissue viscosity sharply dropped (~10-fold) at the onset of doming (Fig. 1f and Supplementary Video 2), suggesting that the blastoderm fluidizes and becomes less resistant to force-induced deformation when doming begins. This fluidization was spatially restricted to central regions of the blastoderm and lasted only until the dome stage, when the blastoderm tissue reaches a uniform thickness (Fig. 1b,f) and radial intercalations become evident (Supplementary Fig. 1a,b). Together, this points to the intriguing possibility that a spatiotemporally restricted tissue fluidization facilitates doming.

Tissue fluidization is essential for early blastoderm spreading. To determine how blastoderm fluidization might function in doming, we first developed a simplified blastoderm-spreading model, in which the deep-cell tissue is represented as a passive fluid, subjected to an external force generated by EVL expansion, driving its elongation (Fig. 1g and Supplementary Fig. 1i). Assuming that blastoderm volume is conserved[19] and fluid viscosity is uniform, the fluid constricts perpendicularly to the elongation axis at a rate set by the elongation speed (Supplementary Note). However, when assuming that viscosity is lower in the centre than at the margin, as experimentally observed, the central region constricted faster than the margin (Fig. 1g, Supplementary Fig. 1j,k and Supplementary Video 3), similar to the blastoderm during doming. This predicts that selective blastoderm fluidization in the centre can explain the characteristic pattern of blastoderm thinning during doming in the absence of radial stress generation. To quantitatively test this prediction, we turned to our fluid dynamic doming model[19], in which the blastoderm is described as an incompressible viscous fluid (Supplementary Note).

[1]Institute of Science and Technology Austria, Klosterneuburg, Austria. [2]The Francis Crick Institute, London, UK. *e-mail: heisenberg@ist.ac.at

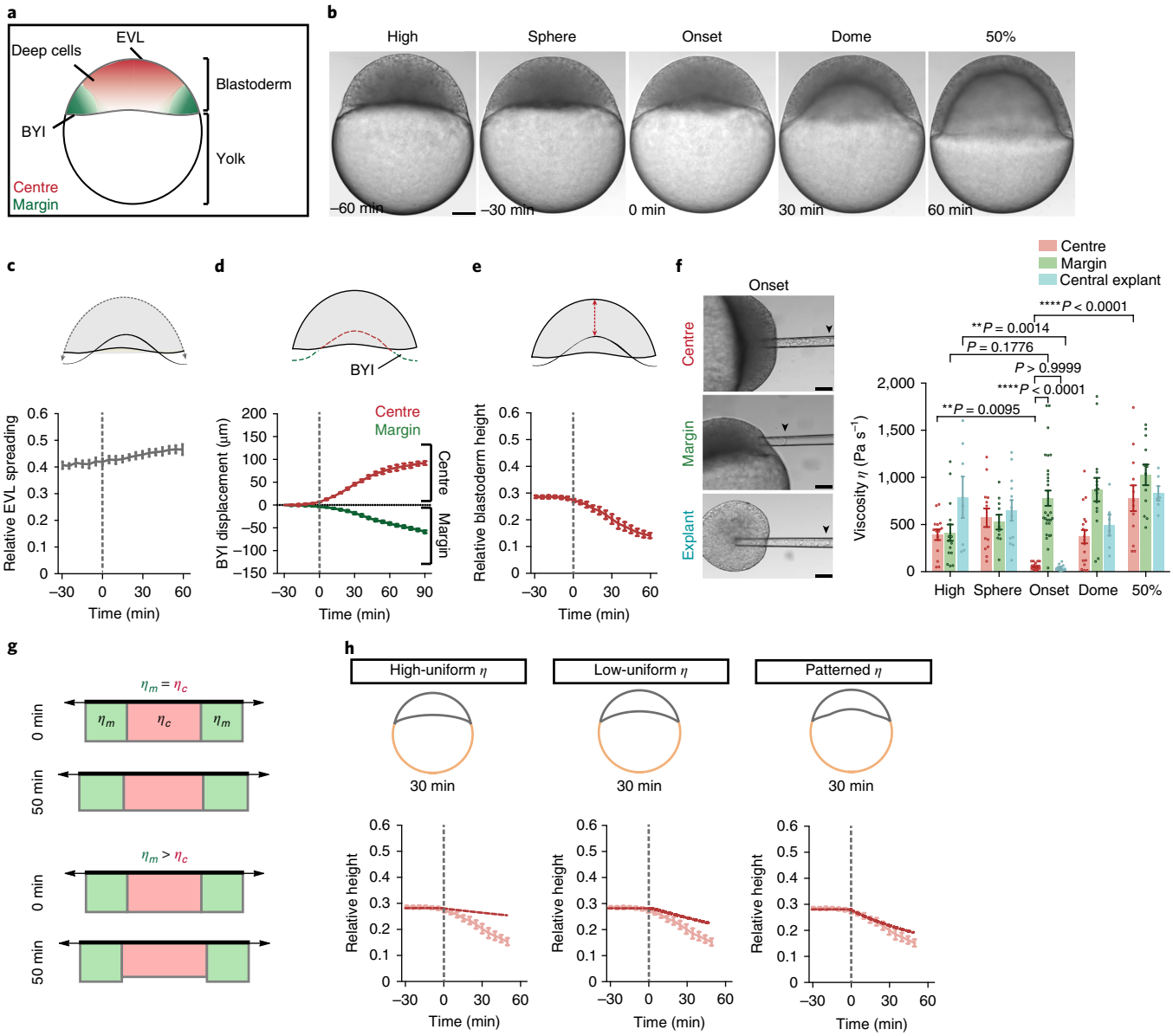

Fig. 1 | Changes in tissue fluidity correlate spatiotemporally with changes in tissue deformation. a, Schematic representation of a sagittal section of a zebrafish embryo at the onset of doming defining the marginal and central blastoderm. **b**, Bright-field single-plane images of an exemplary embryo before (high and sphere stages), during (onset and dome stages) and after doming (50% epiboly stage). **c**, Schematic diagram (top) and plot (bottom) of EVL spreading as a function of time ($n = 8$ embryos). **d**, Schematic diagram (top) of BYI displacement in the central versus marginal blastoderm and plot (bottom) as a function of time ($n = 3$ embryos for centre, 6 embryos for margins). **e**, Schematic diagram (top) and plot (bottom) of the relative central blastoderm height (red double arrow) as a function of time ($n = 4$ embryos). **f**, Bright-field images (left) of exemplary deep-cell aspirations in the blastoderm centre and margin of intact embryos, and in central blastoderm explants at the onset of doming. The black arrowheads indicate cell flow into the micropipette under the same pressure. Bar plot (right) of blastoderm viscosity calculated from the aspiration experiments (centre, $n = 83$ embryos; margin, $n = 81$ embryos; explants, $n = 37$ explants) is also shown. **g**, Shape changes of a three-rectangle system representing the deep-cell tissue as a passive fluid with equal or patterned viscosity (lower in the centre) and subjected to an external constant force by the expanding EVL (black rectangle). **h**, Comparison of experimentally measured (pale red) and simulated (dark red) relative blastoderm height as a function of time for a deep-cell layer with high uniform viscosity (average squared relative deviation (R) = 0.162), low uniform viscosity ($R = 0.089$) and patterned viscosity (~95% reduction in the blastoderm centre; $R = 0.043$), in the presence of surface tissue tension reduction. Experimental data (blastoderm height and central blastoderm viscosity) are taken from **e**,**f**. Simulation parameters are reported in Supplementary Table 1 and obtained in part from ref. [19]. The top panels show simulated embryo shapes at 30 min of doming. In all plots, the onset of doming is indicated with a grey dashed line. Images are representative of ten embryos (**b**) and two (**e**), three (**c**,**d**) or nine (**f**) biological replicates (independent embryo batches). Data are mean ± s.e.m. (**c**–**f**,**h**); Kruskal–Wallis test (**f**). Scale bars, 100 μm (**b**,**f**).

We asked whether the experimentally observed changes in blastoderm viscosity would be sufficient to achieve doming movements in embryos that undergo active EVL expansion but lack radial stress generation (Supplementary Note). Selective, strong (~90%) viscosity reduction within the blastoderm centre, as experimentally observed, led to blastoderm thinning along the symmetry axis that was considerably better at matching the experimental observations than when assuming uniform high or low blastoderm viscosity (Fig. 1h,

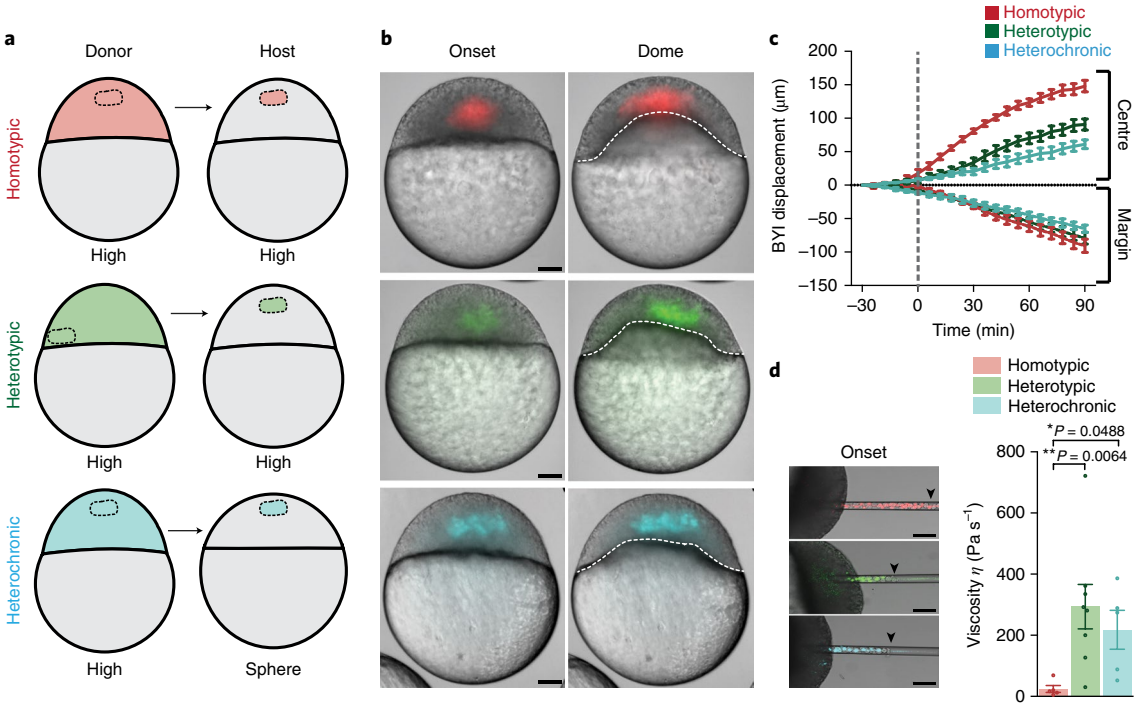

Fig. 2 | Spatiotemporally patterned blastoderm fluidization is required for doming. a, Schematic illustration of homotypic (centre to centre at high stage), heterotypic (margin to centre at high stage) and heterochronic (high-stage centre to sphere-stage centre) deep-cell transplantations. **b**, Exemplary single-plane fluorescence/bright-field images of the transplanted embryos described in **a**, at the onset and end of doming. Transplanted cells are fluorescently marked by H2B-GFP and pseudo-coloured. **c**, BYI displacement in the blastoderm centre containing the transplanted cells versus the margin free of transplanted cells as a function of time during doming (homotypic $n = 7$ transplants; heterotypic $n = 8$ transplants; heterochronic $n = 5$ transplants). The onset of doming is indicated with a grey dashed line. **d**, Bright-field/fluorescent images of exemplary deep-cell aspirations in the transplantation experiments described in **a**. The black arrowheads indicate how far the cells have flown into the micropipette under the same pressure. The bar plot on the right shows tissue viscosity calculated from the deep-cell aspiration experiments in the transplanted area at the onset of doming (homotypic $n = 5$; heterotypic $n = 8$; heterochronic $n = 5$). Images are representative of at least five transplants each (**b**), and three (**c**) or four (**d**) biological replicates (independent embryo batches). Data are mean ± s.e.m. (**c**,**d**); Kruskal–Wallis test (**d**). Scale bars, 100 µm (**b**,**d**).

Supplementary Table 1 and Supplementary Video 4). This suggests that spatially restricted fluidization of the blastoderm centre represents a plausible mechanism controlling blastoderm shape changes at the onset of doming when active force generation is largely restricted to EVL expansion.

To experimentally address the role of tissue fluidization in doming, we first asked whether fluidization is tissue autonomous. To this end, we prepared central blastoderm explants and analysed their viscoelastic properties ex vivo. Remarkably, we found that explants maintained the temporal pattern of viscosity changes as observed for the central blastoderm in intact embryos (Fig. 1f and Supplementary Fig. 1c). Taking advantage of this, we performed deep-cell transplantation experiments to analyse the role of fluidization in doming (Fig. 2a). Specifically, we transplanted deep cells from the blastoderm margin of donor embryos into the blastoderm centre of a host embryo at the same stage (heterotypic), or deep cells from the blastoderm centre of donor embryos into the blastoderm centre of a developmentally advanced host embryo (heterochronic). As controls, we transplanted deep cells from the blastoderm centre of donor embryos into the blastoderm centre of a host embryo at the same stage (homotypic) (Fig. 2a). As fluidization is a deep-cell tissue-autonomous process, we reasoned that, in the heterotypic and heterochronic transplantations, the transplanted tissue would fail to undergo fluidization, allowing us to determine how local impairment of central tissue fluidization affects doming. In all cases, we confirmed through MPA that the transplanted tissue retains its initial viscous properties (Fig. 2d). Strikingly, we found that, only in the heterotypic and heterochronic transplantations, in which transplant fluidization was impaired, central blastoderm thinning at the position of the transplant was reduced (Fig. 2b,c and Supplementary Video 5). This suggests that properly timed and local blastoderm fluidization is required for normal doming movements.

To further test this notion, we interfered with tissue viscosity without varying cell origin and/or developmental stage. Specifically, we induced ectopic deep-cell clustering by transplanting plastic beads coated with the ectodomain of E-cadherin into the blastoderm centre of a host embryo, thereby locally increasing tissue viscosity (Supplementary Fig. 2a,b). In transplanted embryos, blastoderm thinning was reduced in the region of the transplant (Supplementary Fig. 2c,d), further supporting the notion that central tissue fluidization is needed for doming.

Blastoderm fluidization is mediated by destabilization of cell–cell contacts. To elucidate the cellular mechanisms of blastoderm fluidization, we analysed cell cohesion throughout the blastoderm. We found that, at the high stage, both central and marginal deep cells displayed many stable and large cell–cell contacts. However, at the onset of doming, central but not marginal cells gradually decreased their cell–cell contact number, duration and size, accompanied by increased interstitial fluid accumulations between them (Fig. 3a–e and Supplementary Video 6). Notably, this difference in cell–cell contact dynamics and interstitial fluid distribution between central and marginal regions mirrored their fluidity differences (Fig. 1f), suggesting that these phenomena might be

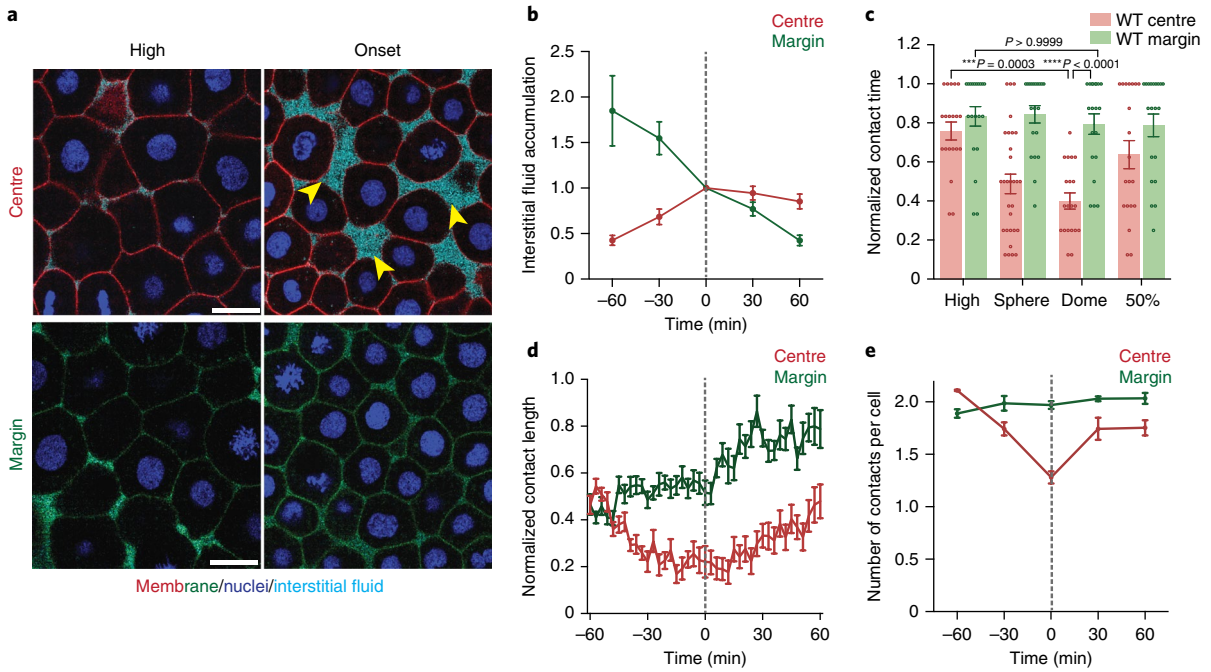

Fig. 3 | Loss of cell–cell contacts coincides with tissue fluidity changes. a, Exemplary high-resolution images of central and marginal deep cells at the high and doming-onset stages. Interstitial fluid accumulations (yellow arrowheads) are marked by dextran, nuclei by H2B-GFP and membranes by membrane RFP (centre, red; margin, green). Scale bars, 20 µm. **b**, Plot of the normalized percentage of interstitial fluid accumulations for central versus marginal regions as a function of time during doming (centre, $n=5$ embryos; margin, $n=5$ embryos). **c**, Bar plot of cell–cell contact time normalized to the total duration of the indicated stages (centre, $n=80$ contacts; margin, $n=80$ contacts). **d**, Plot of cell–cell contact length normalized to cell diameter (for each time point: centre, $n=15$ contacts; margin, $n=15$ contacts). **e**, Plot of the number of cell–cell contacts per cell (centre, $n=1{,}340$ cells; margin, $n=1{,}073$ cells). In all plots, the grey dashed line indicates the onset of doming. Images are representative of four embryos each (**a**) and three (**b**–**e**) independent biological replicates (different embryos). Data are mean ± s.e.m. (**b**–**e**); Kruskal–Wallis test (**c**).

functionally linked. To address this possibility, we initially analysed the role of the interstitial fluid by examining blastoderm fluidity in *poky* (*pky*)-mutant embryos, which exhibit strongly reduced interstitial fluid accumulation and impaired osmolarity due to defective EVL permeability[23] (Supplementary Fig. 3a). Cell–cell contact dynamics and blastoderm fluidization in *pky* mutants exposed to isotonic or hypotonic media were indistinguishable from wild-type (WT) embryos (Supplementary Fig. 3b,c). This suggests that changes in interstitial fluid accumulation and/or osmolarity are unlikely to be the cause for central blastoderm fluidization when doming begins.

To understand why central deep cells lose their contacts when doming starts, we isolated central and marginal deep cells and analysed their cell–cell contact dynamics ex vivo. Consistent with our observation of tissue-autonomous fluidization (Fig. 1f), explanted central but not marginal deep cells gradually disassembled their cell–cell contacts in the same temporal pattern as observed in vivo (Supplementary Fig. 4). This suggests that central deep cell–cell contact disassembly is an intrinsic cell property. Further support for this notion also came from our observation that, in the heterotypic and heterochronic transplants, the duration and size of cell–cell contacts between donor deep cells, which failed to undergo tissue fluidization, were selectively increased compared to the surrounding host deep cells (Figs. 2a and 4a–c).

To elucidate the molecular basis of the difference in cell–cell contact stability between central and marginal deep cells, we analysed the localization and distribution of cell–cell adhesion molecules. We found that E-cadherin[24,25] and associated cortical actin accumulated at the contact edge between deep cells in both the blastoderm centre and at the margin at the high stage (Fig. 4d). However, when doming began, no such distinct accumulation of E-cadherin–actin was detectable anymore in central cells, whereas marginal cells remained unchanged (Fig. 4d). Given that E-cadherin–actin clustering at the contact edge has previously been associated with stable cell–cell contacts[26], this suggests that contact loss in central blastoderm cells is due to intrinsic destabilization of E-cadherin-mediated cell–cell contacts.

Blastoderm tissue fluidization is temporally controlled by the cleavage cycle. To understand how E-cadherin-mediated cell–cell contacts are selectively destabilized in central deep cells, we analysed cell–cell contact dynamics in the context of other cellular processes occurring at the same time. Cell–cell contact disassembly in the blastoderm centre (high stage to doming onset) coincided with the last rounds of metasynchronous cleavages (cell cycle 11–13)[27,28]. Cleavages were associated with mitotic rounding of the dividing cells, reducing cell–cell contact size at metaphase (Fig. 5a,b, Supplementary Fig. 5a and Supplementary Video 7) probably due to the elevated interfacial tension at the cell–cell contact[29,30]. Interestingly, during the last cleavage cycles, mitotic rounding-associated contact disassembly became increasingly more pronounced in central than in marginal deep cells, although the extent of mitotic rounding in marginal cells was indistinguishable from central cells (Fig. 5a,b, Supplementary Fig. 5a,b and Supplementary Video 7). Furthermore, central deep cells failed to reassemble their contacts, whereas marginal cells typically rebuilt them to their initial size (Fig. 5b and Supplementary Fig. 5c). This combination of enhanced contact disassembly and reduced contact reassembly ultimately led to central cells progressively losing their contacts. Collectively, this suggests that successive rounds of cell cleavages trigger progressive central cell–cell contact loss, thereby setting the time of central blastoderm fluidization.

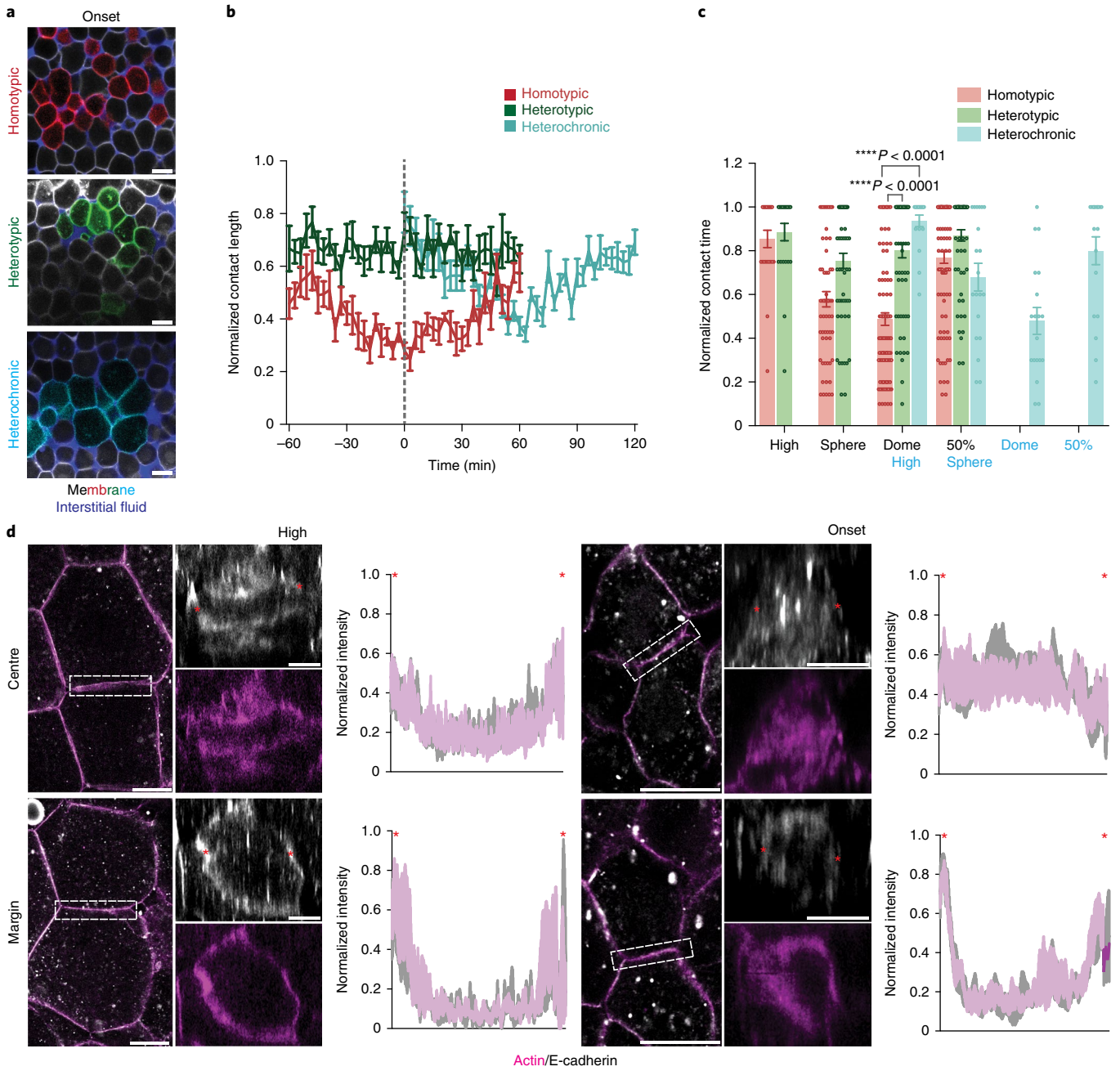

Fig. 4 | Destabilization of E-cadherin contacts is an intrinsic cell property. a, Exemplary confocal images of transplanted donor and host deep cells within the blastoderm centre of the experiments in Fig. 2a at the onset of doming. Donor cells are marked by membrane GFP, host cells by membrane RFP (grey) and interstitial fluid by dextran. **b**, Plot of normalized cell–cell contact length between donor cells (for each time point: homotypic, $n = 8$ cells; heterotypic, $n = 9$ cells; heterochronic, $n = 10$ cells). The grey dashed line indicates the onset of doming. **c**, Bar plot of normalized cell–cell contact time between donor cells (homotypic, $n = 280$ contacts; heterotypic, $n = 215$ contacts; heterochronic, $n = 144$ contacts). At the x axis, the host and heterochronic donor developmental stages are written in black and cyan, respectively. **d**, Exemplary high-resolution images of deep cell–cell contacts in the blastoderm centre versus margin at the high stage and at the onset of doming stained for E-cadherin and phalloidin/actin. Optical sections at the level of the contact (left images) and cross-sections of the contact (right images) outlined by the dashed box are shown. Intensity profiles show the average distribution of E-cadherin and actin across the contact diameter (centre high, $n = 7$ contacts; margin high, $n = 4$ contacts; centre onset, $n = 6$ contacts; margin onset, $n = 6$ contacts). The red asterisks indicate contact edges. Images are representative of three embryos each (**a**) and two (**d**) or three (**b**,**c**) biological replicates (independent embryo batches (**d**); different embryos (**b**,**c**)). Data are mean ± s.e.m. (**b**,**c**,**d**); Kruskal–Wallis test (**c**). Scale bars, 20 µm (**a**,**d**) and 10 µm (cross-sections in **d**).

To directly test this possibility, we inhibited deep-cell cleavages by keeping deep cells in interphase at prefluidization stages and evaluated how this would affect deep-cell cohesion and tissue viscosity. Specifically, we treated embryos at the high stage with the S-phase inhibitor hydroxyurea–aphidicolin (HUA). HUA-treated deep cells failed to undergo their last cleavage cycles and associated mitotic rounding, preventing central cells from disassembling their contacts and the central blastoderm from fluidizing at doming onset

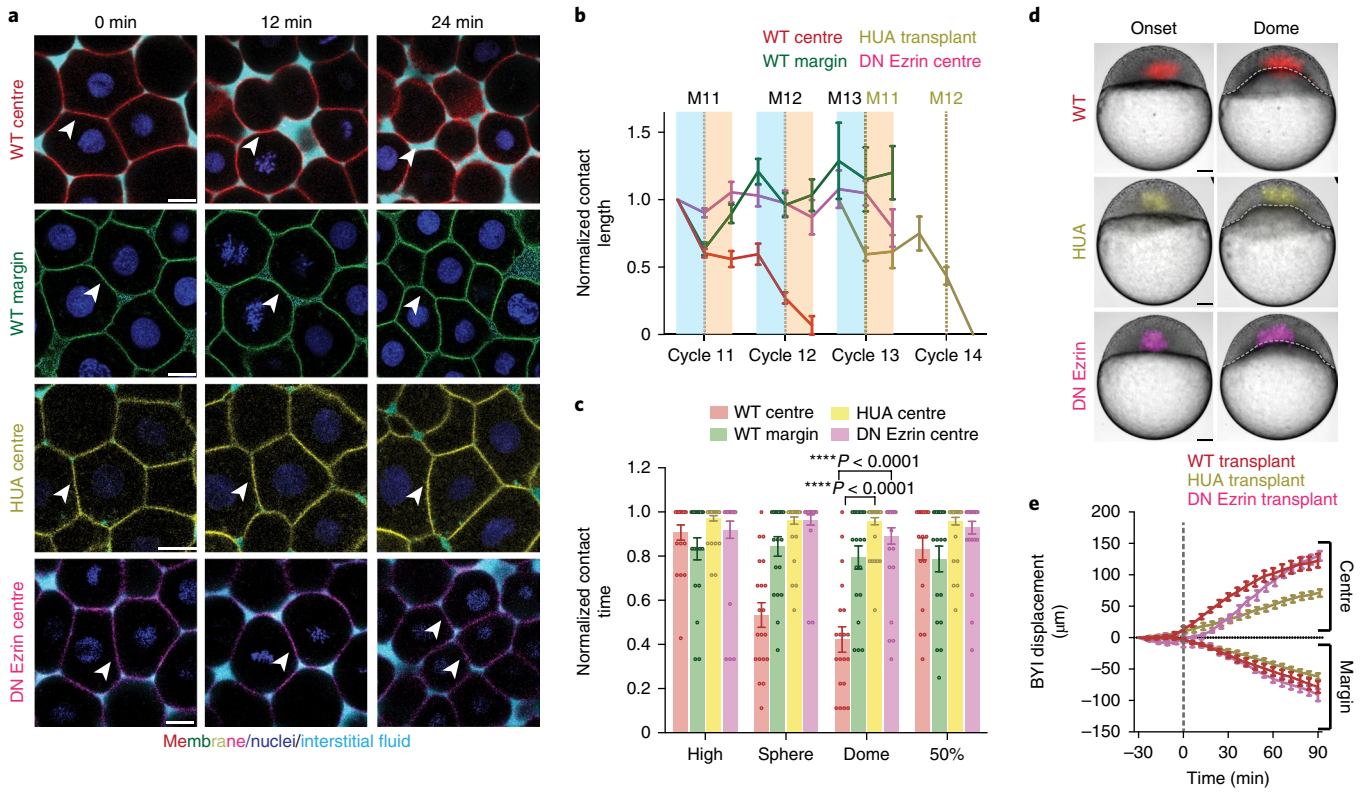

Fig. 5 | Deep-cell cleavage cycle sets the time of central blastoderm fluidization. a, Confocal images of WT central, WT marginal, HUA-treated central and dominant negative (DN) Ezrin-expressing central deep cells. The plasma membrane is labelled by membrane RFP pseudo-coloured in red, green, yellow and magenta, respectively, nuclei by H2B-GFP and interstitial fluid by dextran. The white arrowheads indicate deep cell–cell contacts. **b**, Deep cell–cell contact length normalized to cell diameter plotted at the following time points: 9 min before metaphase, at metaphase and 9 min after metaphase for cycles 11 to 13 for WT central, WT marginal, dominant negative Ezrin-expressing central deep -cells and HUA-treated and transplanted central donor deep cells (WT centre $n=26$ contacts; WT margin $n=16$ contacts; HUA-treated and transplanted centre $n=10$ contacts; dominant negative Ezrin centre $n=20$ contacts). The dashed lines indicate metaphase (M; grey for WT central, WT marginal and dominant negative Ezrin central cells; yellow for HUA-treated and transplanted central cells). The cyan-shaded box outlines the period of contact disassembly. The orange-shaded box outlines the period of contact reassembly. **c**, Bar plot of the deep cell–cell contact time normalized to the total duration of the indicated stages for the different conditions outlined in **a** (WT centre, $n=80$ contacts; WT margin, $n=80$ contacts; HUA centre, $n=160$ contacts; dominant negative Ezrin centre, $n=120$ contacts). **d**, Exemplary single-plane fluorescence/bright-field images of transplanted embryos containing WT, HUA-treated and dominant negative Ezrin-expressing donor central cells in the central WT host blastoderm at the onset and end of doming. Transplanted cells are fluorescently marked by H2B-GFP in red, yellow and magenta, respectively. **e**, BYI displacement as a function of time during doming for the transplanted embryos shown in **d** (WT $n=10$ transplants; HUA $n=6$ transplants; dominant negative Ezrin $n=4$ transplants). The onset of doming is indicated with a grey dashed line. Images are representative of five (**a**) or at least four (**d**) embryos each, and three (**c**,**e**) or four (**b**) biological replicates (different embryos (**b**,**c**); independent embryo batches (**e**)). Data are mean ± s.e.m. (**b**,**c**,**e**); Kruskal–Wallis test (**c**). Scale bars, 20 µm (**a**) and 100 µm (**d**).

(Fig. 5a,c, Supplementary Fig. 5a,d and Supplementary Video 8). To assess the functional relevance of this cleavage-dependent failure in contact disassembly specifically within the deep-cell layer, we transplanted HUA-treated central donor cells (stalled in 10th cycle), into the central blastoderm of untreated host embryos that had completed all cleavage cycles by doming onset. At the time of transplantation, HUA-treated deep cells appeared more cohesive than their neighbouring host cells (Supplementary Fig. 5e), followed by reduced blastoderm thinning in the transplanted area (Fig. 5d,e and Supplementary Video 9). Notably, the transplanted donor cells in the host environment free of HUA eventually restarted cleaving and gradually disassembled their contacts at a stage in which deep-cell tissue cohesion/viscosity in the host embryo had already increased (Fig. 5b and Supplementary Fig. 5b,c,e). Together, this indicates that the final rounds of deep-cell cleavages are required for doming initiation by triggering central deep-cell contact loss and blastoderm fluidization.

To determine whether mitotic rounding is responsible for central deep-cell contact loss as previously suggested for other cells[31], we sought to reduce mitotic rounding without affecting cell cycle progression by interfering with the function of ERM (Ezrin–Radixin–Moesin) proteins required for mitotic rounding[32–34]. Remarkably, central deep cells overexpressing dominant negative Ezrin[32–34] displayed impaired mitotic rounding and reduced cleavage-dependent contact disassembly, leading to larger and more stable contacts by the onset of doming than found in WT cells (Fig. 5a–c and Supplementary Fig. 5a–c). Moreover, when transplanting dominant negative Ezrin-expressing central deep cells into the centre of a WT embryo, the transplanted cells failed to undergo tissue fluidization and, consequently, locally inhibited central blastoderm thinning (Fig. 5d,e and Supplementary Fig. 5f). Together, this suggests that mitotic rounding of deep cells undergoing their final cleavage rounds is required for doming initiation by driving central deep-cell contact loss and blastoderm fluidization.

Wnt11–Frizzled-7 signalling spatially patterns blastoderm fluidization. Our observation that, during cleavage cycle 12 and 13, central but not marginal cells exhibit mitotic rounding-dependent

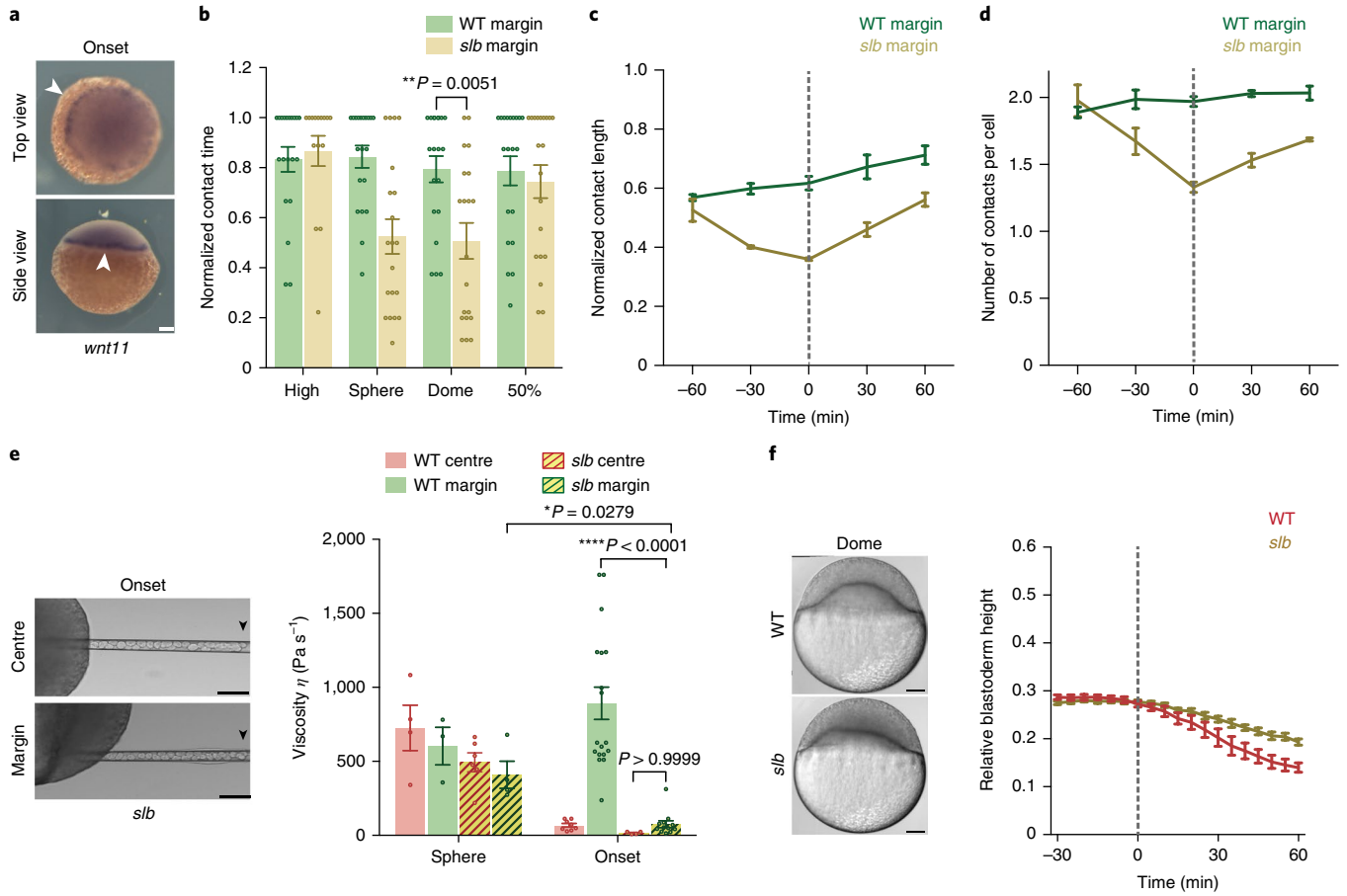

Fig. 6 | Wnt11 signalling suppresses marginal blastoderm fluidization. a, Exemplary top and side views of *wnt11* expression (white arrowheads) in zebrafish embryos at the onset of doming. **b**, Bar plot of cell–cell contact time normalized to the total duration of the indicated stages (WT margin, $n = 80$ contacts; *slb* margin, $n = 75$ contacts). **c**, Plot of cell–cell contact length normalized to cell diameter during doming (for each time point: WT margin, $n = 20$ contacts; *slb* margin, $n = 20$ contacts). **d**, Plot of the number of cell–cell contacts per cell during doming (WT margin, $n = 1{,}073$ cells; *slb* margin, $n = 827$ cells). **e**, Bright-field images of exemplary deep-cell aspirations in the blastoderm centre and margin of *slb*-mutant embryos. The black arrowheads indicate how far the cells have flown into the aspiration pipette under the same pressure. The bar plot on the right shows blastoderm viscosity calculated from the aspiration experiments for the indicated stages (WT centre sphere, $n = 4$ embryos; WT margin sphere, $n = 3$ embryos; WT centre onset, $n = 8$ embryos; WT margin onset, $n = 18$ embryos; *slb* centre sphere, $n = 6$ embryos; *slb* margin sphere, $n = 10$ embryos; *slb* centre onset, $n = 4$ embryos; *slb* margin onset, $n = 12$ embryos). **f**, Bright-field images of representative WT and *slb* embryos at the dome stage. The plot on the right shows the relative blastoderm height as a function of time (WT, $n = 4$ embryos; *slb*, $n = 7$ embryos). The onset of doming is indicated with a grey dashed line (**c**,**d**,**f**). Images are representative of 15 embryos (**a**) and 3 (**b**–**e**) or 4 (**f**) biological replicates (different embryos (**b**–**d**); independent embryo batches (**e**,**f**)). Data are mean ± s.e.m. (**b**–**f**); Kruskal–Wallis test (**b**,**e**). Scale bars, 20 µm (**a**) and 100 µm (**e**,**f**).

tissue fluidization (Fig. 5b and Supplementary Fig. 5b,c) suggests that a reinforcement mechanism might exist within the blastoderm margin that provides mechanical resistance against cleavage-mediated contact loss. Interestingly, the genes encoding the non-canonical Wnt ligand Wnt11 (*wnt11*)[35] (Fig. 6a) and its receptor Frizzled-7 (*fz7*)[36], previously implicated in regulating cell cohesion during zebrafish embryogenesis[36–38], are expressed within the blastoderm margin at doming onset. To address whether non-canonical Wnt signalling might be involved in suppressing mitotic rounding-induced contact loss within the margin, we analysed marginal blastoderm viscosity in *wnt11/slb*-mutant embryos[37]. Strikingly, we found that, at doming onset, not only central but also marginal deep cells from *slb* mutants progressively disassembled their contacts, leading to ectopic marginal tissue fluidization (Fig. 6b–e, Supplementary Fig. 6a–d and Supplementary Video 10). Moreover, *slb* embryos displayed reduced blastoderm thinning (Fig. 6f), consistent with the predictions from doming simulations in embryos with uniform fluidization (Fig. 1h). Similar ectopic contact disassembly and fluidization were observed within the blastoderm margin of mutants for the Wnt11 receptor Fz7 (MZ*fz7a/b*) (Supplementary Fig. 6b–e), suggesting that Wnt11 signals through its receptor Fz7 to provide mechanical resistance against cleavage-mediated contact loss in the margin. To address whether in the absence of Wnt11–Fz7 signalling marginal cells would behave like central cells, we transplanted *slb* and MZ*fz7a/b* marginal cells into the central blastoderm of WT embryos. We found that, contrary to the situation when WT marginal cells were transplanted, transplanted mutant marginal cells allowed central blastoderm thinning to proceed normally by undergoing cell–cell contact disassembly indistinguishable from the surrounding WT central blastoderm (Fig. 7a,b,e,g and Supplementary Fig. 6f–i).

Interestingly, transplanted Wnt11-expressing marginal donor cells failed to influence cell cohesion in the neighbouring host central tissue (Supplementary Fig. 7a), suggesting that central cells might not be competent to respond to Wnt11. To address this, we performed central-to-marginal deep-cell transplantation

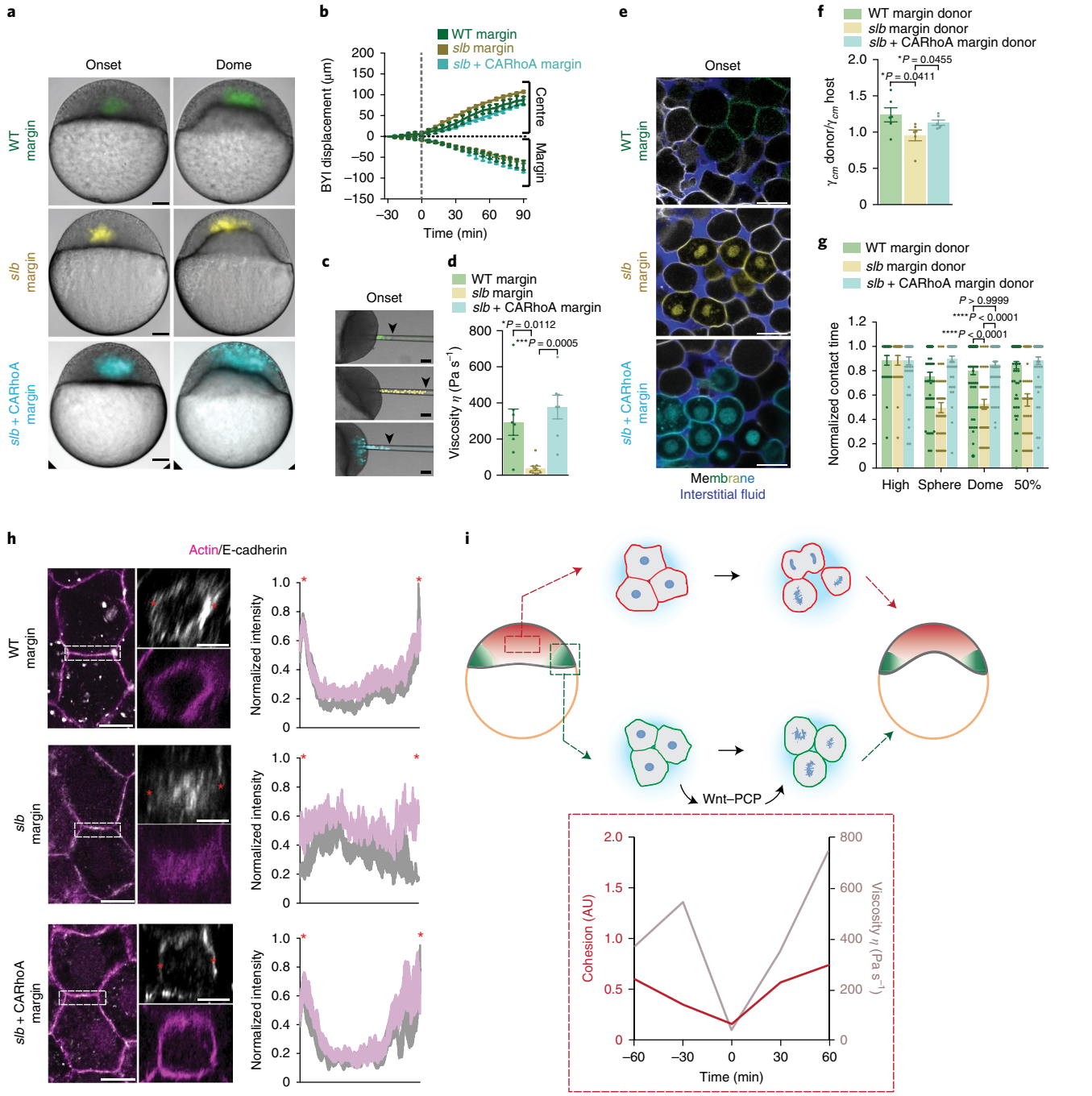

Fig. 7 | Wnt11 signalling prevents marginal blastoderm fluidization by promoting cell cohesion. a, Exemplary single-plane fluorescence/bright-field images of WT, *slb* and *slb*+CARhoA marginal cells (marked by H2B-GFP) transplanted into the WT central blastoderm. **b**, BYI displacement for transplants in **a** (WT, $n=4$ transplants; *slb*, $n=6$ transplants; *slb*+CARhoA, $n=5$ transplants). The grey dashed line indicates doming onset. **c**,**d**, Bright-field/fluorescent images of exemplary aspirations (**c**) and corresponding viscosities (**d**) for the conditions in **a** (WT, $n=8$ transplants; *slb*, $n=10$ transplants; *slb*+CARhoA, $n=7$ transplants). The black arrowheads indicate cell flow into the micropipette under the same pressure. **e**, Exemplary confocal images of the transplants in **a**. Donor cells are marked by membrane GFP, host cells by membrane RFP (grey), nuclei by H2B-GFP (yellow, *slb*; cyan, *slb*+CARhoA) and interstitial fluid by dextran. **f**, Bar plot of the ratio of relative γ_{cm} of donor to host cells for the transplants in **e** (WT, $n=6$ transplants; *slb*, $n=6$ transplants; *slb*+CARhoA, $n=6$ transplants). **g**, Bar plot of normalized cell–cell contact time for the conditions in **e** (WT, $n=240$ contacts; *slb*, $n=160$ contacts; *slb*+CARhoA, $n=200$ contacts). **h**, Exemplary high-resolution images of E-cadherin and phalloidin/actin-stained marginal contacts of WT, *slb* and *slb*+CARhoA embryos at doming onset. Optical sections at the contact level (left) and contact cross-sections (right) are shown. Intensity profiles show the distribution of E-cadherin–actin across the contact (WT, $n=14$ contacts; *slb*, $n=7$ contacts; *slb*+CARhoA, $n=11$ contacts). The red asterisks indicate contact edges. **i**, Schematic of the mechanism defining the spatiotemporal pattern of blastoderm fluidization. Sequential cell cleavages gradually disassemble deep cell–cell contacts, reducing tissue cohesion (see Methods) up to a threshold in which tissue fluidization sets in. Non-canonical Wnt signalling inhibits marginal blastoderm fluidization by stabilizing cell–cell contacts, thereby preventing mitotic rounding-mediated contact disassembly. Images are representative of at least four transplants each (**a**), four embryos each (**e**) and two (**h**) or three (**b**,**d**,**f**,**g**) biological replicates (independent embryo batches (**b**,**d**,**h**); different embryos (**g**)). Data are mean ± s.e.m. (**b**,**d**,**f**,**g**,**h**); Mann–Whitney test (**f**), Kruskal–Wallis test (**d**,**g**). Scale bars, 100 μm (**a**,**c**), 20 μm (**e**), 10 μm (**h**) and 5 μm (cross-sections in **h**).

experiments (Supplementary Fig. 7b). Transplanted central cells displayed ectopic contact loss and fluidization within the margin, resulting in local shape changes of the BYI during doming (Supplementary Fig. 7c–f). This suggests that central cells are unresponsive to Wnt11 signals within the blastoderm margin. Next, we asked whether central cells are unresponsive to Wnt11 signalling because they fail to express the Wnt11 receptor Fz7a[36]. To address this, we ectopically expressed Fz7a in central cells and transplanted them into the blastoderm margin of either WT or *slb* embryos (Supplementary Fig. 7b). Cells transplanted in the blastoderm margin of WT embryos acquired the morphogenetic properties of their surrounding host tissue, whereas cells transplanted in *slb* hosts retained their original properties (Supplementary Fig. 7c–f). This suggests that central deep cells are unresponsive to Wnt11 because they do not express Fz7a.

Wnt11–Fz7 signalling promotes marginal deep-cell cohesion by enhancing actomyosin contractility. Non-canonical Wnt signalling has been previously shown to promote both actomyosin contractility and cell cohesion[36,38,39]. Thus, we speculated that Wnt11–Fz7 signalling prevents cleavage-mediated marginal tissue fluidization by enhancing actomyosin contractility and therefore cell cohesion. To test this possibility, we first asked whether marginal deep cells with active Wnt11–Fz7 signalling are more contractile than central cells. For analysing cell contractility, we performed marginal-to-central transplantations and analysed interfacial tensions to the surrounding interstitial fluid as a readout of cortical actomyosin contractility using 3D video force microscopy (VFM)[40]. This analysis showed that transplanted WT marginal cells displayed higher cortical tension than central cells (Fig. 7f). By contrast, when performing marginal-to-central transplantations using *slb*-mutant cells, no such increased cortical tension was detectable (Fig. 7f). This suggests that Wnt11–Fz7 increases cortical tension in marginal deep cells that might account for their ability to resist cleavage-mediated contact disassembly and fluidization (Fig. 7c–g). Further support for this notion also came from our observation that WT but not *slb* marginal cells displayed distinct E-cadherin–actin localization at cell–cell contact edges (Fig. 7h), previously shown to depend on cortical tension[26].

To directly test whether Wnt11–Fz7 signalling promotes marginal deep-cell contact stability by enhancing cortical tension, we increased cortical tension in *slb* marginal cells by overexpressing constitutively active RhoA (CARhoA) and transplanted those cells into the blastoderm centre of WT embryos. Strikingly, transplanted *slb* marginal deep cells overexpressing CARhoA—similar to WT marginal cells—not only displayed increased cortical contractility and contact stability but also failed to undergo tissue fluidization, leading to reduced blastoderm thinning around the transplanted cells (Fig. 7a–g). Moreover, *slb* marginal cells overexpressing CARhoA showed enhanced localization of E-cadherin and actin at the cell–cell contact edges, which is typically found in stable WT marginal cell–cell contacts (Fig. 7h). Collectively, these results indicate that non-canonical Wnt signalling maintains marginal tissue integrity by enhancing actomyosin contractility, thereby promoting cell–cell contact stability and preventing cleavage-mediated contact loss and tissue fluidization.

Discussion

Regulated changes in tissue viscoelasticity have been proposed to affect tissue morphogenesis in development[5,7,10]. Our findings provide mechanistic insight into the regulation of tissue viscosity within the embryo and how regulated changes in tissue viscosity affect embryo morphogenesis.

Previous studies in chick gastrulation have shown that cell divisions promote epiblast cellular rearrangements[41] and potentially also tissue fluidity. Furthermore, theoretical studies have predicted that the relaxation time of an elastic epithelial tissue is set by the rate of cell divisions[11], suggesting that cell divisions could act on long timescales to relax tissue stress. Our observations suggest that cell divisions can trigger abrupt tissue fluidization on short timescales by driving cell–cell contact disassembly. This provides direct evidence for an important function of cell divisions in tissue fluidization and supports the notion that cell divisions, in addition to promoting tissue growth, have a conserved morphogenetic function in controlling tissue viscosity.

Our finding of Wnt11–Fz7 signalling spatially restricting the effect of cell cleavages on tissue fluidization to the blastoderm centre by promoting cell cohesion within the blastoderm margin (Fig. 7i) is consistent with previous findings of non-canonical Wnt signalling promoting cell cohesion in vertebrate embryogenesis. In mouse embryos, non-canonical Wnt9a signalling has been suggested to influence the final sorting of the inner cell mass by regulating cell cohesion[42,43], whereas in zebrafish embryos, non-canonical Wnt11 signalling is thought to promote collective mesendoderm migration by regulating E-cadherin-mediated adhesion[38,44]. How these effects of non-canonical Wnt signalling on cell cohesion translate in changes of tissue material properties is yet unknown. Cell cohesion has been previously implicated in the regulation of both tissue viscosity and TST[10], pointing to the possibility that cell cohesion affects tissue viscosity by regulating TST. However, our observation that, in the experimental approaches to modulate tissue viscosity, TST (as determined by 3D-VFM[40]) was not recognizably changed (see Methods; Supplementary Table 2 and Supplementary Fig. 7g–i) suggests that cell cohesion affects blastoderm viscosity independently from TST.

Finally, although previous observations suggested that cell cohesion linearly correlates with tissue viscosity[10], our data indicate that, in the zebrafish blastoderm, gradual and small reductions in cell cohesion lead to a sharp drop in tissue viscosity (Fig. 7i). Such abrupt changes in tissue rheology resemble phase transitions, in which a system can change its phase upon small changes in a system parameter[14,45]. This points to the intriguing possibility that tissue phase transitions triggered by small changes in cell cohesion might represent a general regulatory mechanism by which tissues undergo large-scale shape changes.

Online content

Any methods, additional references, Nature Research reporting summaries, source data, statements of data availability and associated accession codes are available at https://doi.org/10.1038/s41556-018-0247-4.

Received: 18 July 2018; Accepted: 2 November 2018;
Published online: 17 December 2018

References

1. Heisenberg, C. P. & Bellaïche, Y. Forces in tissue morphogenesis and patterning. *Cell* **153**, 948–962 (2013).
2. Petridou, N. I., Spiró, Z. & Heisenberg, C. P. Multiscale force sensing in development. *Nat. Cell Biol.* **19**, 581–588 (2017).
3. Gonzalez-Rodriguez, D., Guevorkian, K., Douezan, S. & Brochard-Wyart, F. Soft matter models of developing tissues and tumors. *Science* **338**, 910–917 (2012).
4. Forgacs, G., Foty, R. A., Shafrir, Y. & Steinberg, M. S. Viscoelastic properties of living embryonic tissues: a quantitative study. *Biophys. J.* **74**, 2227–2234 (1998).
5. Lawton, A. K. et al. Regulated tissue fluidity steers zebrafish body elongation. *Development* **140**, 573–582 (2013).
6. Mongera, A. et al. A fluid-to-solid jamming transition underlies vertebrate body axis elongation. *Nature* **561**, 401–405 (2018).
7. Serwane, F. et al. In vivo quantification of spatially varying mechanical properties in developing tissues. *Nat. Methods* **14**, 181–186 (2017).
8. Moore, S. W., Keller, R. E. & Koehl, M. A. The dorsal involuting marginal zone stiffens anisotropically during its convergent extension in the gastrula of *Xenopus laevis*. *Development* **121**, 3131–3140 (1995).

9. Shook, D. R., Kasprowicz, E. M., Davidson, L. A. & Keller, R. Large, long range tensile forces drive convergence during *Xenopus* blastopore closure and body axis elongation. *eLife* **7**, e26944 (2018).
10. David, R. et al. Tissue cohesion and the mechanics of cell rearrangement. *Development* **141**, 3672–3682 (2014).
11. Ranft, J. et al. Fluidization of tissues by cell division and apoptosis. *Proc. Natl Acad. Sci. USA* **107**, 20863–20868 (2010).
12. Stirbat, T. V. et al. Fine tuning of tissues' viscosity and surface tension through contractility suggests a new role for α-catenin. *PLoS ONE* **8**, e52554 (2013).
13. Bi, D., Lopez, J. H., Schwarz, J. M. & Manning, M. L. A density-independent rigidity transition in biological tissues. *Nat. Phys.* **11**, 1074–1079 (2015).
14. Bi, D., Yang, X., Marchetti, M. C. & Manning, M. L. Motility-driven glass and jamming transitions in biological tissues. *Phys. Rev. X* **6**, 1–13 (2016).
15. Angelini, T. E. et al. Glass-like dynamics of collective cell migration. *Proc. Natl Acad. Sci. USA* **108**, 4714–4719 (2011).
16. Sadati, M., Taheri Qazvini, N., Krishnan, R., Park, C. Y. & Fredberg, J. J. Collective migration and cell jamming. *Differentiation* **86**, 121–125 (2013).
17. Bruce, A. E. E. Zebrafish epiboly: spreading thin over the yolk. *Dev. Dyn.* **245**, 244–258 (2016).
18. Lepage, S. E. & Bruce, A. E. E. Zebrafish epiboly: mechanics and mechanisms. *Int. J. Dev. Biol.* **54**, 1213–1228 (2010).
19. Morita, H. et al. The physical basis of coordinated tissue spreading in zebrafish gastrulation. *Dev. Cell* **40**, 354–366.e4 (2017).
20. Davidson, L. A. Embryo mechanics: balancing force production with elastic resistance during morphogenesis. *Curr. Top. Dev. Biol.* **95**, 215–241 (2011).
21. Guevorkian, K., Colbert, M. J., Durth, M., Dufour, S. & Brochard-Wyart, F. Aspiration of biological viscoelastic drops. *Phys. Rev. Lett.* **104**, 1–4 (2010).
22. Guevorkian, K. & Maître, J. L. Micropipette aspiration: a unique tool for exploring cell and tissue mechanics in vivo. *Methods Cell Biol.* **139**, 187–201 (2017).
23. Fukazawa, C. et al. *poky/chuk/ikk1* is required for differentiation of the zebrafish embryonic epidermis. *Dev. Biol.* **346**, 272–283 (2010).
24. Song, S. et al. Pou5f1-dependent EGF expression controls E-cadherin endocytosis, cell adhesion, and zebrafish epiboly movements. *Dev. Cell* **24**, 486–507 (2013).
25. Shimizu, T. et al. E-cadherin is required for gastrulation cell movements in zebrafish. *Mech. Dev.* **122**, 747–763 (2005).
26. Maitre, J.-L. et al. Adhesion functions in cell sorting by mechanically coupling the cortices of adhering cells. *Science* **338**, 253–256 (2012).
27. Mendieta-Serrano, M. A., Schnabel, D., Lomelí, H. & Salas-Vidal, E. Cell proliferation patterns in early zebrafish development. *Anat. Rec.* **296**, 759–773 (2013).
28. Kimmel, C. B., Ballard, W. W., Kimmel, S. R., Ullmann, B. & Schilling, T. F. Stages of embryonic development of the zebrafish. *Dev. Dyn.* **203**, 253–310 (1995).
29. Sorce, B. et al. Mitotic cells contract actomyosin cortex and generate pressure to round against or escape epithelial confinement. *Nat. Commun.* **6**, 8872 (2015).
30. Stewart, M. P. et al. Hydrostatic pressure and the actomyosin cortex drive mitotic cell rounding. *Nature* **469**, 226–231 (2011).
31. Théry, M. & Bornens, M. Get round and stiff for mitosis. *HFSP J.* **2**, 65–71 (2008).
32. Rosenblatt, J. Mitosis: moesin and the importance of being round. *Curr. Biol.* **18**, 1–6 (2015).
33. Carreno, S. et al. Moesin and its activating kinase Slik are required for cortical stability and microtubule organization in mitotic cells. *J. Cell Biol.* **180**, 739–746 (2008).
34. Tachibana, K., Haghparast, S. M. A. & Miyake, J. Inhibition of cell adhesion by phosphorylated ezrin/radixin/moesin. *Cell Adhes. Migr.* **9**, 502–512 (2015).
35. Makita, R., Mizuno, T., Koshida, S., Kuroiwa, A. & Takeda, H. Zebrafish *wnt11*: pattern and regulation of the expression by the yolk cell and no tail activity. *Mech. Dev.* **71**, 165–176 (1998).
36. Witzel, S., Zimyanin, V., Carreira-Barbosa, F., Tada, M. & Heisenberg, C. P. Wnt11 controls cell contact persistence by local accumulation of Frizzled 7 at the plasma membrane. *J. Cell Biol.* **175**, 791–802 (2006).
37. Heisenberg, C.-P. et al. Silberblick/Wnt11 mediates convergent extension movements during zebrafish gastrulation. *Nature* **405**, 76–81 (2000).
38. Ulrich, F. et al. Slb/Wnt11 controls hypoblast cell migration and morphogenesis at the onset of zebrafish gastrulation. *Development* **130**, 5375–5384 (2003).
39. Dzamba, B. J., Jakab, K. R., Marsden, M., Schwartz, M. A. & DeSimone, D. W. Cadherin adhesion, tissue tension, and noncanonical Wnt signaling regulate fibronectin matrix organization. *Dev. Cell* **16**, 421–432 (2009).
40. Brodland, G. W. et al. CellFIT: a cellular force-inference toolkit using curvilinear cell boundaries. *PLoS ONE* **9**, e99116 (2014).
41. Firmino, J., Rocancourt, D., Saadaoui, M., Moreau, C. & Gros, J. Cell division drives epithelial cell rearrangements during gastrulation in chick. *Dev. Cell* **36**, 249–261 (2016).
42. Meilhac, S. M. et al. Active cell movements coupled to positional induction are involved in lineage segregation in the mouse blastocyst. *Dev. Biol.* **331**, 210–221 (2009).
43. Xenopoulos, P., Kang, M. & Hadjantonakis, A.-K. Cell lineage allocation within the inner cell mass of the mouse blastocyst. *Results Probl. Cell Differ.* **55**, 185–202 (2012).
44. Ulrich, F. et al. Wnt11 functions in gastrulation by controlling cell cohesion through Rab5c and E-cadherin. *Dev. Cell* **9**, 555–564 (2005).
45. Schoetz, E.-M., Lanio, M., Talbot, J. A. & Manning, M. L. Glassy dynamics in three-dimensional embryonic tissues. *J. R. Soc. Interface* **10**, 20130726 (2013).

Acknowledgements

We thank O. Campas and members of the Heisenberg laboratory for technical advice and discussions, and the Bioimaging and zebrafish facilities of the IST Austria for continuous support. This work was supported by a postdoctoral fellowship from EMBO Long-term fellowships to N.I.P. (ALTF-534 2016) and an ERC Advanced Grant (MECSPEC) to C.-P.H. S.G. and G.S. were supported by The Francis Crick Institute, which receives its core funding from Cancer Research UK (FC001317), the UK Medical Research Council (FC001317) and the Wellcome Trust (FC001317).

Author contributions

N.I.P. and C.-P.H. designed the research. N.I.P. performed the experiments and analysed the experimental data. G.S. and S.G. developed the theoretical doming models. S.G. performed the doming simulations. E.H. analysed the cell cohesion and tissue rigidity data. N.I.P. and C.-P.H. wrote the manuscript.

Competing interests

The authors declare no competing interests.

Additional information

Supplementary information is available for this paper at https://doi.org/10.1038/s41556-018-0247-4.

Reprints and permissions information is available at www.nature.com/reprints.

Correspondence and requests for materials should be addressed to C.-P.H.

Publisher's note: Springer Nature remains neutral with regard to jurisdictional claims in published maps and institutional affiliations.

Methods

Zebrafish handling. Zebrafish (*Danio rerio*) were maintained under a 14-h light/10-h dark cycle[46]. The following zebrafish strains were used in this study: WT AB, *Tg(actb2:Lifeact-EGFP)*[47], *Tg(actb2:GFP-Has.UTRN)*[47], *slb/MZwnt11*[37], MZ*fz7ab* (MZ*fzd7a* e3/*fzd7b* hu2986)[48] and *pky*[49]. Zebrafish embryos were grown at 25–28.5 °C in E3 embryo medium and staged as previously described[50]. For precise staging before and during doming, the last rounds of metasynchronous cleavages and resulting changes in cell size were used as temporal hallmarks, defining developmental time relative to the onset of doming. Embryonic manipulations of WT embryos were performed in 1× Danieau's solution (58 mM NaCl, 0.7 mM KCl, 0.4 mM $MgSO_4$, 0.6 mM $Ca(NO_3)_2$ and 5 mM HEPES (pH 7.2)). For experiments on *pky* embryos (Supplementary Fig. 3), 1× Danieau's solution was used as hypotonic medium (~120 mOsm l^{-1}) and 1× Ringer's (116 mM NaCl, 2.9 mM KCl, 1.8 mM $CaCl_2$ and 5 mM HEPES (pH 7.2)) as isotonic medium (~258 mOsm l^{-1}). All animal experiments were carried out along the guidelines of the Ethics and Animal Welfare Committee (ETK) in Austria.

Embryo microinjections. Zebrafish embryos were injected using glass capillary needles (30-0020, Harvard Apparatus), which were pulled by a needle puller (P-97, Sutter Instrument) and attached to a microinjector system (PV820, World Precision Instruments). Microinjections of mRNAs were performed at the one-cell stage. mRNAs were synthesized using the mMACHINE SP6 kit (Ambion). The following mRNAs were injected: 70 pg membrane green fluorescent protein (GFP)[51], 70 pg membrane red fluorescent protein (RFP)[52], 70 pg H2A mCherry[53], 70 pg H2B GFP[54], 250 pg dominant negative Ezrin (T564A)[55], 100 pg Fz7a-Neon[36] and 2 pg CARhoA (RhoA V14)[56]. To label the interstitial fluid, 1 nl of 0.6 mg ml^{-1} dextran Alexa Fluor 647 (10,000 MW; D22914, Invitrogen) was injected in the blastoderm of 1k-cell-stage embryos (~3 h post-fertilization).

Explants. Central blastoderm explants for MPAs were prepared in 1× Danieau's solution by dechorionating donor embryos with forceps and excising animal pole regions of the blastoderm (excluding the margin) with a hair-knife. Explants were left to round up for 30 min at 25 °C prior to aspiration.

Deep-cell transplantations. Donor and host embryos were dechorionated with forceps and transferred into 1× Danieau's embryo medium. For all of the transplantation conditions, a bevelled fire-polished transplantation needle with a 45-µm inner diameter (Biomedical Instruments) attached to a syringe system was used. For the homotypic transplantations, approximately 3 nl deep cells (~5% of the blastoderm volume) were removed either from the central or marginal region of the blastoderm of a high-stage donor embryo and transplanted to the central or marginal region of the blastoderm of a high-stage host embryo, respectively. For the heterotypic transplantations, approximately 3 nl deep cells were removed either from the marginal or central region of the blastoderm of a high-stage donor embryo and transplanted to the central or marginal region of the blastoderm of a high-stage host embryo, respectively. For the heterochronic transplantations, approximately 3 nl deep cells were removed from the central region of the blastoderm of a high-stage donor embryo and transplanted to the central region of the blastoderm of a sphere-stage host embryo. For the bead transplantations, approximately 30 E-cadherin-coated beads were transferred with a transplantation needle into the central blastoderm of high-stage host embryos.

Isolation and ex vivo culture of deep cells. Deep-cell isolation was performed in pre-warmed (25 °C) CO_2-independent DMEM/F-12 medium (11039-021, Sigma) as follows: for isolating central deep cells, the blastoderm of 1k-cell-stage embryos was excised from the yolk cell and the deep-cell tissue in the blastoderm centre was shaved off the EVL using a hair-knife. For isolating marginal deep cells, the blastoderm of 1k-cell-stage embryos was excised from the yolk cell, the remaining yolk was removed from marginal regions of the blastoderm and deep-cell tissue from the blastoderm margin was shaved off the EVL using a hair-knife. A mixture of either central or marginal deep-cell tissues from 10 embryos was transferred with a serum-coated 10-µl micropipette into a 1.5-ml Eppendorf tube containing DMEM/F-12. Upon slight shaking, deep cells were dissociated and transferred onto glass coverslips passivated with 1% BSA and coated with 3% methylcellulose (M0387, Sigma).

Bead coating. For coating, protein A-conjugated 4% agarose beads of an average diameter of 17 µm (customized product, ABT-Agarose Bead Technologies) were washed twice in 1× PBS, then incubated with 50 µg ml^{-1} mouse E-cadherin/Fc chimera (E2153, Sigma) for 1 h at room temperature, washed three times in 1× PBS, incubated with 10 µg ml^{-1} of rabbit Alexa Fluor 546 anti-goat secondary antibody (A-21085, Thermo Fisher Scientific) for 30 min at room temperature, washed three times in 1× PBS and diluted in 10 µl of 1× Danieau's solution.

Block of cell division. Dechorionated embryos were treated with a cocktail of 60 mM hydroxyurea (H8627, Sigma) and 300 µM aphidicolin (A0781, Sigma) from the 1-k-cell stage onwards.

MPA and viscosity/surface tension measurements. Blastoderm viscosity was measured by MPA based on previously established protocols[18]. Briefly, embryos were placed on 3% methylcellulose coated glass coverslips in 1× Danieau's solution (or 1× Ringer's when stated) on an inverted Leica SP5 microscope. A fire-polished, passivated (with heat-inactivated FBS) micropipette of 25-, 35- and 45-µm inner diameter, 30° bent, with a spike end (Biomedical Instruments) was inserted into the central or marginal blastoderm, just below the EVL. The micropipette movements were controlled by motorized micromanipulators (TransferMan Nk2, Eppendorf). Upon insertion of the pipette in the blastoderm, aspiration pressure of 250, 200 or 150 Pa, depending on the pipette size, (Supplementary Fig. 1e-f) was immediately applied using a Microfluidic Flow Control System Pump (Fluiwell, Fluigent) (with negative pressure ranging from 7 to 750 Pa, a pressure accuracy of 7 Pa and change rate of 200 Pa s^{-1}) and the Dikeria micromanipulation software. Pressure was applied until the tissue flew into the pipette at a constant velocity (for ~5 min, except for the cases in which the tissue was fluidized and the deformation was too fast) and then pressure was immediately released. Images were acquired every 500 ms, monitoring the aspiration and relaxation of the tissue. When aspirating transplants, only cases in which more than 50% of the aspirated tissue was consisting of transplanted cells were taken into consideration for the viscosity measurements. During the aspiration, no wound response was observed neither in the EVL nor in the aspirated deep cells (Supplementary Fig. 1h). Yolk viscosity was measured using a micropipette with a 35-µm inner diameter, a 30° bent and a spike, which was inserted in the middle of the yolk at the onset of doming. EVL viscosity was measured using a micropipette with a 25- or 40-µm inner diameter, a 30° bent and a straight end, which was applied on the surface of the EVL during doming. Viscosity calculations were performed as previously described[21,22]. Briefly, the tongue length for each time point was measured using a customized Fiji macro, and changes in tongue length during aspiration and relaxation were then plotted over time (Supplementary Fig. 1d). The slope of the aspiration curve (L_{asp}) at the point of constant flow depends on the viscosity η, $L_{asp} = R_p(\Delta P - P_c)/3\pi\eta$, with R_p being the radius of the pipette, ΔP the applied pressure and P_c the critical pressure. When the pressure is set to zero during the relaxation, the tissue retracts at a velocity $L_{ret} = R_p(P_c)/3\pi\eta$. From the aspiration and retraction rates, viscosity can be calculated as $\eta = R_p \Delta P/3\pi(L_{asp} + L_{rel})$. In case the retraction rates are very low, then the major determinant of viscosity is the aspiration rate. Notably, although a faster relaxation would be expected for lower η given that L_{ret} is inversely proportional to η, this is not detectable when comparing central (low η) versus marginal (high η) blastoderm tissues at the onset of doming owing to the very low surface tension of the central tissue as judged by MPA (calculated with $\gamma = P_c/2R_p$; Supplementary Fig. 1g). Notably, the actual surface tension of deep cells within the blastoderm is even lower than the surface tension measured by MPA, considering that, in the MPA experiments, surface tension of deep cells at their interface to the buffer within the pipette is analysed, whereas within the blastoderm, deep cells are not completely surrounded by fluid but also form cell–cell contacts with the EVL and yolk cell (see also '3D-VFM/CellFIT-3D analysis' and Supplementary Fig. 7g–i).

3D-VFM/CellFIT-3D analysis. To obtain the relative distribution of interfacial tensions of host and donor deep-cell tissues in the transplantation experiments, the angles at triple edges between host (labelled by membrane GFP), donor (labelled by membrane RFP) and interstitial fluid (labelled by dextran Alexa Fluor 647) were measured along multiple images from confocal z-stacks (3-µm interval) in transplanted embryos using custom software as described[40,57,58]. Force balance equations were written for each triple edge, and least-squares solutions were found for all equations. The solutions of these equations provided the coordinates and calculations of the relative interfacial tensions along each edge type.

Validation of 3D-VFM/CellFIT-3D analysis. To clarify that 3D-VFM is a valid method for measuring interfacial tension within the embryo, TST of marginal and central deep-cell tissues obtained by using either 3D-VFM or MPA was compared. When using MPA, the TST of the probed deep-cell tissue at its interface to the buffer within the pipette is measured. By contrast, when using 3D-VFM in intact and internal tissues, the TST of the probed deep-cell tissue at its interfaces with both medium and other surrounding cells is measured. To provide a common and thus comparable interface of the probed tissues in both the MPA and the 3D-VFM measurements, marginal and central deep-cell tissues for the 3D-VFM measurements were placed in culture medium/buffer, thereby mimicking the situation in the MPA measurements in which the probed tissue faces the buffer in the micropipette. In such comparable conditions, the relative TST of marginal versus central deep-cell tissues obtained by either 3D-VFM or MPA assays was similar (Supplementary Fig. 7g–i), supporting the notion that 3D-VFM can be used to measure TST within the embryo.

Immunostaining. Embryos were fixed in 2% paraformaldehyde for 4 h at room temperature. After fixation, they were washed in 0.5% Tween-20 (in 1× PBS) overnight at 4 °C, dechorionated and washed in 0.5% Tween-20, 0.5% Triton X-100 and 0.1 M glycine (in 1× PBS) for 1 h at room temperature. Embryos were then incubated in blocking solution (0.5% Tween-20, 0.5% Triton X-100, 1% dimethylsulfoxide and 1% BSA in 1× PBS) for 3–4 h at room temperature and then incubated with the primary antibody (rabbit E-cadherin anti-zebrafish[52], 1:200, generated at Max Planck Institute of Molecular Cell Biology and Genetics, Dresden, Germany) diluted in the blocking solution overnight at 4 °C. Embryos

were subsequently washed 4×20 min in 0.5% Tween-20 and incubated with the secondary antibody (goat Alexa Fluor 546 anti-rabbit, 1:500, A11010, Thermo Fisher Scientific) and Phalloidin Alexa Fluor 488 (1:500, A12379, Thermo Fisher Scientific) diluted in the blocking solution overnight at 4 °C. Finally, embryos were washed 4×20 min in 0.5% Tween-20, post-fixed in 4% paraformaldehyde for 30 min at room temperature and imaged.

In situ hybridization. In situ hybridization was performed as previously described[59]. In situ probes were synthesized from cDNA for *wnt11* (ref. [37]), using the DIG RNA-labelling kit (11 277 073 910, Sigma).

Image acquisition. Dechorionated embryos were mounted in 0.5% low melting point agarose (16,520-050, Invitrogen) on a glass-bottom dish (P35G-1.5-14-C, MatTek Corporation). Mounted embryos were kept in an incubation chamber at 28.5 °C throughout acquisition. Whole-embryo single-plane bright-field/fluorescence imaging was performed on a Nikon Eclipse inverted wide-field microscope equipped with CFI Plan Fluor ×10/0.3 objective (Nikon) and a fluorescent light source (Lumencor). For high-magnification confocal imaging of deep cells, a Zeiss LSM880 inverted microscope, equipped with a Plan-Apochromat ×40/NA 1.2 water-immersion objective (Zeiss), a Plan-Apochromat ×63/NA 1.4 oil-immersion objective (Zeiss), GaAsP and multialkali PMT detectors and Fast Airyscan super-resolution, was used. For imaging the MPA experiments, a Leica SP5 inverted microscope equipped with a resonant scanner and a HC Plan-Apochromat ×10/NA 0.4 objective (Leica) was used.

Data analysis and quantification. All acquisition data were processed using Fiji (NIH), ilastik and/or Imaris 9.0. EVL spreading (Fig. 1c) was measured as h_b/h_t, with h_b being the height of the blastoderm from the top region of the embryo to the meeting point of EVL, BYI and yolk (as described in ref. [19]) and h_t being the total height of the embryo. This ratio was calculated every 5 min. BYI displacement was quantified as schematized in Fig. 1d. Specifically, the position of the BYI at the sphere stage was set to zero. Using the multi-point tool in Fiji, the position of the BYI in each time point (6-min interval) was marked on the *y* axis in the centre (positive displacement) and at the margins (negative displacement, measured at a 50-µm distance from the EVL margin). In the deep-cell transplanted embryos, central BYI displacement was quantified in a similar manner, selecting a point on the BYI positioned below the central transplant. Marginal BYI displacement was measured in a region entirely consisting of non-transplanted host marginal cells. In the bead transplantations, central BYI displacement in the non-transplanted (control) and transplanted sides was measured in the same embryo as schematized in Supplementary Fig. 2d. For quantifying marginal BYI displacement in the bead-transplanted embryos, the margin at the bead-transplanted side was considered as 'bead marginal BYI', whereas the other side was considered as the 'control marginal BYI'. Tissue thinning was quantified as schematized in Fig. 1e. Blastoderm thickness in the centre of the embryo was measured as h_c/h_t, with h_c being the height of the blastoderm in the centre (indicated by the red double-headed arrow in Fig. 1e from the centre top region of the embryo to the BYI) and h_t being the total height of the embryo (extending the same arrow to the bottom of the yolk cell). This ratio was calculated every 5 min. The shape of the BYI at the dome stage in the marginal transplantation experiments was evaluated as shown in the diagram of Supplementary Fig. 7f. The angle formed between the marginal and central tissue was measured by drawing two virtual lines: one line originating at the contact point of marginal EVL and BYI and extending along the BYI until the BYI changed direction, and one from the point the BYI changed direction and extending along the BYI new direction. Deep-cell protrusion orientation relative to the radial axis of the blastoderm was quantified as schematized in Supplementary Fig. 1a, and actin intensity was measured in an region of interest at the cell edges intersecting the radial or lateral axis. The percentage of cell divisions within the deep-cell layer was determined by dividing the number of dividing deep cells by the total number of deep cells in 2D at the indicated time points. Relative interstitial spaces labelled by dextran Alexa Fluor 647 were quantified on confocal images of the first four deep-cell layers of the blastoderm within central and marginal blastoderm regions (Fig. 3b). A region of interest of the same size for both regions and each cell layer was selected, and using ilastik to segment interstitial fluid from cells, an intensity threshold was automatically determined for each image. This threshold was then used in Fiji to create a binary image, in which the percentage of pixels above this threshold was considered as fluid and below as cells. For each cell layer, the interstitial fluid percentage was normalized to that at the onset of doming. Cell–cell contact time was quantified as follows: neighbouring deep cells from embryos labelled for the membrane and interstitial fluid were followed over time (3-min interval) until deep cell–cell contact disassembly was identified by the presence of interstitial fluid between the cells. The total contact time was expressed as a percentage of the total recording time for each stage (~30 min). In the transplanted embryos, only the contacts between the donor deep cells were analysed. Cell–cell contact length was quantified as follows: the contact length of neighbouring membrane-labelled deep cells was normalized to the average cell diameter of the contacting cells. Contact length was defined by the length of the cell–cell interface free of interstitial fluid. Cell–cell contact length analysis was performed in a 3-min time interval. In the transplanted embryos, only the contacts between the donor deep cells were analysed. The cell–cell contact number was defined on 2D confocal images in which the nuclei, cell–cell contacts and interstitial fluid accumulations were differentially labelled. Cell nuclei of cells within the same focal plane that had no interstitial fluid between them were considered as contacting cells. To extract the average contact number per cell, the number of contacts was divided by the total number of cells in the image. Notably, the average number of contacts per cell appears less than what is shown on the image owing to the fact that the shared contacts are counted only once. To estimate deep cell–cell cohesion in Fig. 7i, the average number of contacts was multiplied with the average contact time and the average contact size of central deep cells at high, sphere, onset, dome and 50% epiboly stages. For the distribution of adhesion proteins at the cell–cell contact, the images were first processed using the Airyscan mode (Zeiss). 3D reconstructions and cross-sections of the contact surface were performed by Imaris 9.0. The intensity profiles of E-cadherin and actin at the contact surface were made using the line tool of 20-pixel thickness in Fiji. The intensity values for the proteins shown were normalized to the maximum intensity value across each contact. For quantifying the clustering of deep cells around E-cadherin-coated beads, interstitial fluid accumulation was measured as shown in Supplementary Fig. 2a. The average intensity of the interstitial fluid (labelled with dextran Alexa Fluor 647) was measured in regions of interest (with an approximate width the size of a cell diameter) directly adjacent and further away (50 µm) from the bead. Mitotic rounding was quantified by measuring the length-to-width ratio (aspect ratio) of interphase and metaphase deep cells at the plane of the DNA. Contact length relative to the cell cycle phase was analysed as follows: the same contact was followed over time from the interphase of cell cycle 11 (3-min time interval) onwards and the contact length was measured as described above for the following time points: 9 min before metaphase (t_{bm}), at metaphase (t_m) and 9 min after metaphase (t_{am}) from cycle 11 to 13. The data were normalized to the length of the contact at the first time point. For evaluating cell–cell contact disassembly in each cell cycle, the data were normalized to the length (L) of the contact at t_{bm} and disassembly (D) was expressed as $D = L_{bm} - L_m$. For evaluating the effect of cell cleavage on contact size for each cell cycle, the data were normalized to the length of the contact at t_{bm} and reassembly (R) was expressed as $R = L_{am} - L_{bm}$.

Statistics and reproducibility. The statistical analyses were performed with GraphPad Prism 6.0. Statistical details of experiments are reported in the figures and figure legends. Sample size is reported in the figure legends and no statistical test was used to determine sample size. The biological replicate is defined as the number of embryos or independent batches of embryos, as stated in the figure legends. No inclusion/exclusion or randomization criteria were used and all analysed samples are included. Unless differently stated in the figure legends, the graphs show mean ± s.e.m. and the error bars are calculated and shown based on the number of cells or embryos, as indicated. The statistical test used to assess significance is stated in the figure legends and was chosen after testing each group with the normality distribution test D'Agostino. For comparing two groups, a two-tailed Student's *t*-test for parametric distributions and a Mann–Whitney *U*-test for non-parametric distributions were used. To compare more than two groups either an analysis of variance (ANOVA) or Kruskal–Wallis test for parametric and non-parametric distributions, respectively, was used. No blind allocations were used during the experiments or in the analysis. At least more than three independent experiments were performed except for the data shown in: Figs. 1e, 4d, and 7h and Supplementary Figs. 2b,d, 4, 5f (embryos from two different embryo batches, in which an independent experiment was defined as the embryo batch) and 7a (cells from two different embryos, in which an independent experiment was defined as the different embryos). This information is also stated in the figure legends. All details on statistical analysis are reported in 'Statistics source data' in Supplementary Table 3.

Reporting Summary. Further information on research design is available in the Nature Research Reporting Summary linked to this article.

Code availability. The Fiji macro used to quantify the MPA experiments is available upon request. Simulations are available from the corresponding author upon request. The coordinates of the interfacial tension vectors and a script to extract the raw angles from the 3D-VFM analysis are available from the corresponding author upon request.

Data availability

Source data for Figs. 1c–f, 2c,d, 3b–e, 4b–d, 5b,c,e, 6b–f and 7b,d,f–h and Supplementary Figs. 1b–g, 2a,b,d, 3b,c, 4, 5a–d,f, 6b–e,h,i and 7a,d–f,h,i have been provided as Supplementary Table 3. All other data supporting the findings of this study are available from the corresponding author upon request.

References

46. Detrich, W. H. I., Westerfield, M. & Zon, L. I. (eds) *The Zebrafish: Biology* (Academic Press, Cambridge, 1999).
47. Behrndt, M. et al. Forces driving epithelial spreading in zebrafish gastrulation. *Science* **338**, 257–260 (2012).

48. Quesada-Hernández, E. et al. Stereotypical cell division orientation controls neural rod midline formation in zebrafish. *Curr. Biol.* **20**, 1966–1972 (2010).
49. Wagner, D. S., Dosch, R., Mintzer, K. A., Wiemelt, A. P. & Mullins, M. C. Maternal control of development at the midblastula transition and beyond: mutants from the zebrafish II. *Dev. Cell* **6**, 781–790 (2004).
50. Kimmel, C. B. & Law, R. D. Cell lineage of zebrafish blastomeres. I. Cleavage pattern and cytoplasmic bridges between cells. *Dev. Biol.* **108**, 78–85 (1985).
51. Kimmel, R. A. & Meyer, D. Molecular regulation of pancreas development in zebrafish. *Methods Cell Biol.* **100**, 261–280 (2010).
52. Iioka, H., Ueno, N. & Kinoshita, N. Essential role of MARCKS in cortical actin dynamics during gastrulation movements. *J. Cell Biol.* **164**, 169–174 (2004).
53. Arboleda-Estudillo, Y. et al. Movement directionality in collective migration of germ layer progenitors. *Curr. Biol.* **20**, 161–169 (2010).
54. Keller, P. J., Schmidt, A. D., Wittbrodt, J. & Stelzer, E. H. K. Reconstruction of zebrafish early embryonic development by scanned light sheet microscopy. *Science* **322**, 1065–1069 (2008).
55. Ruprecht, V. et al. Cortical contractility triggers a stochastic switch to fast amoeboid cell motility. *Cell* **160**, 673–685 (2015).
56. Jopling, C. & den Hertog, J. Fyn/Yes and non-canonical Wnt signalling converge on RhoA in vertebrate gastrulation cell movements. *EMBO Rep.* **6**, 426–431 (2005).
57. Krens, S. F. G. et al. Interstitial fluid osmolarity modulates the action of differential tissue surface tension in progenitor cell segregation during gastrulation. *Development* **144**, 1798–1806 (2017).
58. Brodland, G. W. et al. Video force microscopy reveals the mechanics of ventral furrow invagination in *Drosophila*. *Proc. Natl Acad. Sci. USA* **107**, 22111–22116 (2010).
59. Thisse, C., Thisse, B., Halpern, M. E. & Postlethwait, J. H. Goosecoid expression in neurectoderm and mesendoderm is disrupted in zebrafish cyclops gastrulas. *Dev. Biol.* **164**, 420–429 (1994).

nature research

Corresponding author(s): Carl-Philipp Heisenberg

Reporting Summary

Nature Research wishes to improve the reproducibility of the work that we publish. This form provides structure for consistency and transparency in reporting. For further information on Nature Research policies, see Authors & Referees and the Editorial Policy Checklist.

Statistical parameters

When statistical analyses are reported, confirm that the following items are present in the relevant location (e.g. figure legend, table legend, main text, or Methods section).

n/a	Confirmed	
☐	☒	The exact sample size (*n*) for each experimental group/condition, given as a discrete number and unit of measurement
☐	☒	An indication of whether measurements were taken from distinct samples or whether the same sample was measured repeatedly
☐	☒	The statistical test(s) used AND whether they are one- or two-sided *Only common tests should be described solely by name; describe more complex techniques in the Methods section.*
☒	☐	A description of all covariates tested
☐	☒	A description of any assumptions or corrections, such as tests of normality and adjustment for multiple comparisons
☐	☒	A full description of the statistics including central tendency (e.g. means) or other basic estimates (e.g. regression coefficient) AND variation (e.g. standard deviation) or associated estimates of uncertainty (e.g. confidence intervals)
☐	☒	For null hypothesis testing, the test statistic (e.g. *F*, *t*, *r*) with confidence intervals, effect sizes, degrees of freedom and *P* value noted *Give P values as exact values whenever suitable.*
☒	☐	For Bayesian analysis, information on the choice of priors and Markov chain Monte Carlo settings
☒	☐	For hierarchical and complex designs, identification of the appropriate level for tests and full reporting of outcomes
☒	☐	Estimates of effect sizes (e.g. Cohen's *d*, Pearson's *r*), indicating how they were calculated
☐	☒	Clearly defined error bars *State explicitly what error bars represent (e.g. SD, SE, CI)*

Our web collection on statistics for biologists may be useful.

Software and code

Policy information about availability of computer code

Data collection	No software was used for data collection
Data analysis	Fiji (NIH), imaris 9.0, ilastik, CellFIT-3D, GraphPad Prism 6.0

For manuscripts utilizing custom algorithms or software that are central to the research but not yet described in published literature, software must be made available to editors/reviewers upon request. We strongly encourage code deposition in a community repository (e.g. GitHub). See the Nature Research guidelines for submitting code & software for further information.

Data

Policy information about availability of data

All manuscripts must include a data availability statement. This statement should provide the following information, where applicable:

- Accession codes, unique identifiers, or web links for publicly available datasets
- A list of figures that have associated raw data
- A description of any restrictions on data availability

Source data for Fig. 1c,d,e,f; 2c,d; 3b,c,d,e; 4b,c,d; 5b,c,e; 6b,c,d,e,f; 7b,d,f,g,h and Supplementary Fig. 1b,c,d,e,f,g; 2a,b,d; 3b,c; 4; 5a,b,c,d,f; 6b,c,d,e,h,i; 7a,d,e,f,h,i have been provided as Supplementary Table 3. All other data supporting the findings of this study are available from the corresponding author upon request.

Field-specific reporting

Please select the best fit for your research. If you are not sure, read the appropriate sections before making your selection.

☒ Life sciences ☐ Behavioural & social sciences ☐ Ecological, evolutionary & environmental sciences

For a reference copy of the document with all sections, see nature.com/authors/policies/ReportingSummary-flat.pdf

Life sciences study design

All studies must disclose on these points even when the disclosure is negative.

Sample size	No sample size calculation was performed. Sample size is different in each experiment. All samples sizes are reported in figure legends. Sample size was chosen based on our previous experience and the work of other groups using zebrafish embryos as a model system. (Nature Cell Biology 19, 306-317, 2017) (Developmental Cell 40, 354-366, 2017)
Data exclusions	No data were excluded from the analysis
Replication	All attempts at replication were successful. At least more than three independent experiments were performed except for the data shown in: Fig. 1e, Fig. 4d, Fig. 7h, Supplementary Fig. 2b, d, Supplementary Fig. 4, Supplementary Fig. 5f (embryos from two different embryo batches, where an independent experiment was defined as the embryo batch) and Supplementary Fig. 7a (cells from two different embryos, where an independent experiment was defined as the different embryos). This information is also stated in the figure legends.
Randomization	No randomization methods were used to determine how samples/organisms were allocated.
Blinding	No blind allocations during data collections and/or analysis was relevant to the study. The nature of the experiments in this study requires the investigators to not be blinded to group allocation in order to describe and identify the mechanistic determinants of tissue fluidization

Reporting for specific materials, systems and methods

Materials & experimental systems

n/a	Involved in the study
☐	☒ Unique biological materials
☐	☒ Antibodies
☒	☐ Eukaryotic cell lines
☒	☐ Palaeontology
☐	☒ Animals and other organisms
☒	☐ Human research participants

Methods

n/a	Involved in the study
☒	☐ ChIP-seq
☒	☐ Flow cytometry
☒	☐ MRI-based neuroimaging

Unique biological materials

Policy information about availability of materials

Obtaining unique materials	All unique materials used are readily available from the authors or from standard commercial sources (zebrafish E-cadherin antibody; Biomedical instruments for custom-made micropipettes; Agarose beads technologies for custom-made beads).

Antibodies

Antibodies used	Rabbit zebrafish specific anti-E-cadherin, 1:200 (generated at Max Planck Institute of Molecular Cell Biology and Genetics). goat Alexa Fluor 546 anti-rabbit, 1:500, A11010 ThermoFisher Scientific phalloidin Alexa Fluor 488, 1:500, A12379, ThermoFisher Scientific rabbit Alexa Fluor 546 anti-goat, 10 ug/ml, A-21085 ThermoFisher Scientific
Validation	The E-cadherin specific antibody was validated through immunostaining in zebrafish embryos (Koppen, M., et al., Development, 2006; Montero, J.-A., et al., 2005).

Animals and other organisms

Policy information about studies involving animals; ARRIVE guidelines recommended for reporting animal research

Laboratory animals	Danio rerio zebrafish strains [WT AB; Tg(actb2:Lifeact-EGFP); Tg(actb2:GFP-Has.UTRN); slb / MZ wnt11; MZ fz7ab (MZ fzd7a e3/ fzd7b hu2986)] at adult (7-20 months) and embryonic stages (until 6 hours post fertilization) were used. Female and male adult fish were used for natural mating. The sex of the embryos used is unknown.
Wild animals	No wild animals were used.
Field-collected samples	No field collected samples were used.